PAPER

Check for updates

How oxidation state and lattice distortion influence the oxygen evolution activity in acid of iridium double perovskites†

María Retuerto,[*a] Laura Pascual,[b] Oriol Piqué,[c] Paula Kayser,[d] Mohamed Abdel Salam,[e] Mohamed Mokhtar,[e] José Antonio Alonso,[d] Miguel Peña,[a] Federico Calle-Vallejo[c] and Sergio Rojas[*a]

In view of iridium's scarceness and high cost, Ir-containing catalysts for water electrolyzers should have low loadings and maximal utilization. Here, we studied low-Ir-content, highly active, double perovskites (Sr_2MIrO_6, M = Ni, Co, Sc and Fe) for the oxygen evolution reaction (OER) in acid combining electrochemical experiments, DFT, and advanced characterization techniques. The initial OER performance depends on Ir's oxidation state and the geometric features of IrO_6 frameworks, which are tuned by the choice of M. Higher oxidation states, particularly Ir^{6+}, enhance the OER activity: Sr_2NiIrO_6 and Sr_2CoIrO_6 display potentials of ∼1.53 V at 10 mA cm^{-2}, comparable to the best Ir-based catalysts in the literature. However, because of their less symmetric structures, perovskites with Ir^{6+} are less stable, prone to surface reconstruction and their cations leach under OER conditions. These results show that improved iridium-based OER electrocatalysts in acid can be designed by balancing their activity and stability.

1. Introduction

Hydrogen is a versatile energy carrier, capable of paving the way for the energy transition toward a decarbonized economy. It can enable the penetration of renewable electricity in sectors conventionally coupled to fossil fuels such as transportation, heat, (petro)chemicals, iron and steel, thereby substantially reducing carbon emissions.[1,2] Polymer Membrane Water Electrolyzers (PEMWE) are among the most suitable technologies to accumulate the surplus of renewable energy into H–H chemical bonds.[3] Because PEMWEs are versatile, have fast-response and are modular devices able to work at high current densities to yield high-purity hydrogen, they are suitable to cope with the intrinsic intermittency of renewable energy.[4]

Water electrolysis comprises two half reactions: the formation of hydrogen at the cathode (in acid: $4H^+ + 4e^- \rightarrow 2H_2$, hydrogen evolution reaction, HER) and the formation of oxygen at the anode (in acid: $2H_2O \rightarrow O_2 + 4H^+ + 4e^-$, oxygen evolution reaction, OER).[5] In acidic media, the overall process is limited by the sluggish kinetics of the OER[6] and the highly corrosive environment associated with water electrolysis. As a consequence, iridium- and ruthenium-based oxides are the state-of-the-art catalysts for the OER.[4] Ru-based oxides typically display the lowest OER overpotentials; however, their stability in acid is insufficient.[7] Therefore, benchmark catalysts are based on IrO_2 and IrO_2/TiO_2,[8,9] yielding current densities of 10 mA cm^{-2} at ∼1.52 V and mass activities of ∼30–50 A g^{-1} at 1.5 V.[10–12]

Since Ir is one of the rarest, ill-distributed and most expensive elements on the Earth's crust, traded in a volatile market where slight fluctuations in demand can significantly impact supply,[13] it is necessary to make the best possible utilization of it. In this sense, mixed oxides are promising candidates to replace pure iridium oxides as electrocatalysts for the OER.[14–17] For instance, the mass percentage of Ir in IrO_2 is 86 wt%, and goes down to 59 wt% in $SrIrO_3$ and 36–38 wt% in Sr_2MIrO_6, if M is a first-row transition metal. To the best of our knowledge, the iridium mixed oxides with OER activity in acid electrolyte reported so far are: (i) Ir-based perovskites such as $SrIrO_3/IrO_x$ thin films,[18,19] $SrCo_{0.9}Ir_{0.1}O_3$,[20] Ba_2RIrO_6 (R = Y, La, Ce, Pr, Nd, Tb),[21,22] La_2LiIrO_6,[23] 6H-$SrIrO_3$,[24] Ir–$SrTiO_3$,[25] Sr_2FeIrO_6 and Sr_2CoIrO_6,[26] (ii) Ir–pyrochlores such as $Bi_2Ir_2O_7$, $Pb_2Ir_2O_{6.5}$,[27]

aGrupo de Energía y Química Sostenibles, Instituto de Catálisis y Petroleoquímica, CSIC, C/Marie Curie 2, 28049, Madrid, Spain. E-mail: m.retuerto@csic.es; srojas@icp.csic.es

bInstituto de Catálisis y Petroleoquímica, CSIC, C/Marie Curie 2, 28049, Madrid, Spain

cDepartament de Ciència de Materials i Química Física, Institut de Química Teòrica i Computacional (IQTCUB), Universitat de Barcelona, Martí i Franquès 1, 08028 Barcelona, Spain

dInstituto de Ciencia de Materiales de Madrid, CSIC, C/ Sor Juana Inés de la Cruz 3, 28049 Madrid, Spain

eDepartment of Chemistry, Faculty of Science, King Abdulaziz University, P.O Box 80200, Jeddah 21589, Saudi Arabia

$Pr_2Ir_2O_7$,[28] $Y_2Ir_2O_7$,[29] (iii) spinels such as $Ni_{0.34}Co_{0.46}Ir_{0.2}O_4$,[30] and (iv) Ruddlesden–Popper phases such as Sr_2IrO_4 and Sr_4IrO_6.[31]

Looking at the performance of the aforementioned compounds, we hypothesize that the OER activity of Ir mixed oxides is related to the actual environment of Ir cations in such oxides. In other words, the OER activity is likely affected by the nature of the foreign metal(s) and the actual location of the cations in the oxides. However, the roles of the foreign metals, the crystal structure including conformation, the distortions, the bond strength of the IrO_6 octahedra (Oh), and that of Ir's oxidation state on the OER performance of Ir mixed oxides, are not fully understood. Evidently, this knowledge void prevents the rational design of advanced Ir-based OER electrocatalysts.

A number of studies suggest a direct relationship between the environment and oxidation state of Ir in its oxides and their OER activity.[25,30] The most usual Ir oxidation states in oxides are +3 and +4, as in Sr_2TaIrO_6, Sr_2NbIrO_6,[32] and Sr_2TiIrO_6.[33] However, such perovskites present cationic disorder with Ta, Nb or Ti and Ir randomly occupying the same crystallographic position, thereby preventing the study of the actual role of Ir's environment for the OER. A recent study illustrated the relevance of upper iridium oxides for the OER.[22] Oxides with Ir^{5+} or Ir^{6+} are less common; however, double perovskites with Ir cations in upper oxidation states have been reported, for instance, Ba_2RIrO_6 (R = Ce, Tb, Y, La, Pr, Nd),[21] La_2LiIrO_6,[23] $Sr_2(Fe,Co)IrO_6$ (ref. 26) and $Sr_2(Ca, Mg)IrO_6$.[34] These double perovskites exhibit cationic ordering between R, Li, Fe, Co, Ca or Mg and Ir; being Ir cations located in an independent crystallographic position than the other metals, which allows studying the impact of Ir's environment for the OER.

The suitability of OER electrocatalysts should be assessed holistically by studying their catalytic performance, including activity, durability and stability. It is well known that the activity depends on the oxygen adsorption strength of the active sites. This strength depends on several factors, such as the position of the oxygen's p-band with respect to the Fermi level, which determines the hybridization between M d orbitals and O 2p orbitals.[35] In turn, the degree of hybridization is tuned by the transition metal oxidation state, the number of d electrons and the electronegativity of the metal ions.[36,37] Another essential parameter to evaluate the quality of an OER catalyst is its durability. Several factors concerning the stability of mixed oxides at the harsh conditions of the OER in acid media should be considered. The first factor is the distortion of the crystal structure. For perovskites, large size differences between the cations in the A and B positions usually implies large deviations from the cubic symmetry and a marked destabilization of the mixed oxide structure under the high potentials of the OER.[36] The second factor is the leaching of the non-noble components of the perovskite into the electrolyte, leading to severe reconstruction of the catalyst during the OER along with the formation of amorphous IrO_x/IrOOH phases at the catalyst surface. In some cases, the reconstruction is fast and happens after only few OER cycles, or even upon immersion in the electrolyte, before the commencement of the OER experiments.[20,22,23,38]

In this work, we aim at establishing sound correlations between representative structural parameters of Ir perovskites, namely IrO_6 Oh distortion and Ir oxidation state, and the strength of the metal–adsorbate bonds. Furthermore, we assess the effects of those structural and energetic parameters on the OER performance. We carefully tune the environment and oxidation state of Ir in double perovskites, Sr_2MIrO_6, by changing the nature of the M cations (M = Ni, Co, Sc, Fe). This strategy allows us to find correlations between a variety of parameters, the initial OER activity, and the stability of Sr_2-$MIrO_6$, all of which provide insights for the design of improved Ir-based electrocatalysts.

2. Experimental section

2.1 Synthesis of Sr_2MIrO_6 perovskites

The synthesis of Sr_2MIrO_6 (M = Ni, Co, Sc, Fe) is detailed elsewhere.[33,39] Briefly, the samples were prepared by sol–gel methods. We used a solution of citric acid and HNO_3 to dissolve the starting materials. IrO_2 was not dissolved but stayed in suspension under magnetic stirring. The suspension was slowly evaporated leading to organic resins containing a homogeneous distribution of the involved cations. After evaporation, the resins were dried at 140 °C and heated at 600 °C for 12 h to decompose the organic materials and nitrates. Next, Sr_2NiIrO_6 was annealed at 900 °C for 12 h in O_2 flow and subsequently at 900 °C under 200 bar of O_2 for 48 h, to obtain the Ir^{6+} perovskite oxide. For Sr_2MIrO_6 (M = Co, Sc, Fe) oxides the reactive precursors were heated in air at 1100 °C for 12 h.

2.2 Physicochemical characterization

The phase identification and purity of the obtained perovskites was determined by X-ray powder diffraction (XRD) in the Bragg–Brentano reflection geometry with CuK_{α} radiation ($\lambda = 1.5418$ Å). A detailed study of the crystal structure using Powder Neutron Diffraction (PND) and the analysis of Ir oxidation states and coordination environments using X-ray Absorption Spectroscopy (XAS) is available in the literature.[33,39]

Transmission Electron Microscopy (TEM), high-resolution electron microscopy (HRTEM) and X-ray energy dispersive spectra (EDX) were recorded in a 200 kV (JEOL 2100F) field emission gun transmission electron microscope equipped with an EDX X-Max 80 spectrometer (Oxford Instruments). The specimens were prepared by depositing aliquots onto a Cu grid supporting a lacey carbon film.

X-ray photoelectron spectra (XPS) were acquired with a VG ESCALAB 200 R at a pass energy of 50 eV using a Mg Kα X-ray source. The kinetic energies of the photoelectrons were measured using a hemispherical electron analyser working in the constant-pass energy mode. A background pressure below 3 × 10^{-8} mbar was kept in the chamber during data acquisition. The binding energies were determined by setting the C 1s peak at 284.6 eV. 200 scans in increments of 0.1 eV with dwell times of 50 ms were collected in order to increase the signal-to-noise ratio.

This journal is © The Royal Society of Chemistry 2021

J. Mater. Chem. A, 2021, **9**, 2980–2990 | **2981**
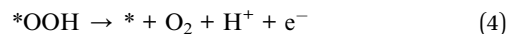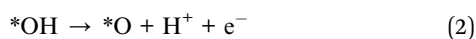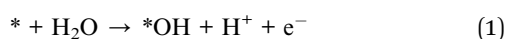
2.3 Electrochemical characterization

An Autolab PGstat 302N potentiostat/galvanostat was used to test the electrochemical performance of the oxides. The measurements were performed using a standard three-compartment glass cell and a rotating disk electrode (RDE) (Pine Research Instruments). A graphite bar was used as counter electrode. An Ag/AgCl electrode was used as reference electrode. The perovskites were deposited as an ink on a 0.196 cm^2 glassy carbon electrode. The ink was prepared by mixing 5 mg of oxide with 1 mg of carbon black (Vulcan-XC-72R) to improve the electrical conductivity. The mixture was dispersed in tetrahydrofuran (THF) and 5% Nafion and sonicated using an Ultrasonic Processor UP50H (Hielscher). The composition of the ink was 5 mg_{oxide}, 1 mg_{vulcan}, 0.03 mL_{Nafion} and 0.97 mL_{THF}. 10 μL of the ink were dropped onto the electrode to obtain a catalyst loading of 0.255 mg_{oxide} cm^{-2}, or $\sim$0.09 mg_{Ir} cm^{-2}, depending on the oxide.

The OER catalytic performance of the perovskites was evaluated by recording linear sweep voltammograms between 1.1 and 1.7 V at 10 mV s^{-1}. The measurements were performed in an O_2 saturated 0.1 M $HClO_4$ electrolyte to assure the O_2/H_2O equilibrium at 1.23 V, at a rotation rate of 1600 rpm. The OER kinetic curves were capacitance-corrected by using the average of the anodic and cathodic curves and iR-corrected by using the formula $E - iR_{corrected} = E_{applied} - iR$, where i is the current and R is the uncompensated resistance ($R \sim 29\ \Omega$) as obtained from Electrical Impedance Spectroscopy (EIS) at open voltage.

Durability tests were performed by recording 50 consecutive OER cycles at 10 mV s^{-1} between 1.2 and 1.7 V $vs.$ RHE, or by chronoamperometric tests by fixing the initial potential for each catalyst to the potential needed to reach 10 mA cm^{-2} and monitoring the evolution of the current density with time. The durability of Sr_2NiIrO_6 and Sr_2CoIrO_6 was further tested by recording 10 000 consecutive cycles between 1.2 and 1.7 V at 50 mV s^{-1}.

2.4 Computational details

The VASP code was used to perform the DFT calculations,[40] RPBE was the chosen exchange-correlation functional,[41] and the projector augmented-wave (PAW) method was used to describe the effect of the inner cores on the valence electron density.[42] The free energies of reaction were approximated as $\Delta G \approx \Delta E_{DFT} + \Delta ZPE - T\Delta S$, where ΔE_{DFT} is the DFT-calculated reaction energy and ΔZPE is the zero-point energy change between reactants and products. The ZPEs were obtained from vibrational frequency calculations using the harmonic approximation. As usual,[43,44] the term $T\Delta S$ includes the total entropies of the molecules involved in the OER, and neglects those of the adsorbates. The computational hydrogen electrode (CHE) was used to model proton–electron pairs.[45] We assumed the following catalytic pathway for the OER:[43,44]

$$* + H_2O \rightarrow *OH + H^+ + e^- \tag{1}$$

$$*OH \rightarrow *O + H^+ + e^- \tag{2}$$

$$*O + H_2O \rightarrow *OOH + H^+ + e^- \tag{3}$$

$$*OOH \rightarrow * + O_2 + H^+ + e^- \tag{4}$$

Within the CHE framework, the free energies of reaction can be written as a function of the adsorption energies of the three adsorbed intermediates, namely *O, *OH, and *OOH:

$$\Delta G_1 = \Delta G_{OH} \tag{5}$$

$$\Delta G_2 = \Delta G_O - \Delta G_{OH} \tag{6}$$

$$\Delta G_3 = \Delta G_{OOH} - \Delta G_O \tag{7}$$

$$\Delta G_4 = \Delta G_{O_2} - \Delta G_{OOH} \tag{8}$$

where $\Delta G_{O_2} = 4.92$ eV corresponds to the standard equilibrium potential ($E^0 = 1.23$ V) multiplied by the total number of electrons per catalytic cicle (1.23 V $\times$ 4e^- = 4.92 eV). The adsorption energies of *O, *OH and *OOH are defined using $H_2O(l)$ and proton–electron pairs and are provided in Table S1† for the perovskites under study. We extracted from the free energies in eqn (5)–(8) the potential-limiting step, which determines the calculated OER overpotential (η_{OER}):[43,44]

$$\eta_{OER} = \max(\Delta G_1, \Delta G_2, \Delta G_3, \Delta G_4)/e^- - 1.23\ V \tag{9}$$

As shown in previous publications,[46,47] the concept of electrocatalytic symmetry as expressed by the electrochemical-step symmetry index (ESSI) is a good descriptor for the OER overpotential:

$$ESSI = \frac{1}{n} \sum_1^n \left(\frac{\Delta G_i^+}{e^-} - E^0 \right) \tag{10}$$

where ΔG_i^+ corresponds to the reaction energies in eqn (5)–(8) larger than 1.23 eV.

A full description of δ–ε optimization can be found elsewhere.[47] Briefly, the method is based on the introduction of two parameters into the adsorption energies: (I) δ, which is scaling-based and affects *O, *OH and *OOH, and (II) ε, which is scaling-free and affects *OOH only. Both parameters are in units of energy. Normally, reasonable values for δ are in the range [−0.3, 0.3] eV, whereas those of ε are in the range [−0.3, 0] eV. δ is either a weakening or strengthening of the adsorption energies, while ε is only a strengthening. See Section S2 of the ESI† for more details and the specific values obtained for the double perovskites containing Ni and Co.

We note that there are known inaccuracies of DFT for the OER modelling of some oxides $e.g.$ RuO_2,[48,49] and some solutions have been proposed.[48,50,51] In particular, the inaccuracies of DFT observed before for $SrIrO_3$ (ref. 19) were corrected for in this study by using thick slabs. For further information on the computational details please refer to Section S1 of the ESI.†

3. Results and discussion

3.1 Double-perovskite structure and composition

The incorporation of different M metals into Sr_2MIrO_6 is expected to result in materials with different structural and chemical features, namely unit-cell volume, Ir oxidation state,

Ir–O and M–O bond lengths, structural distortions, *etc.* In the following, we intend to disclose the effect of those features on the OER performance of iridium mixed oxides. Fig. S1 in the ESI† shows the XRD diffractograms for Sr_2MIrO_6 (M = Ni, Co, Sc and Fe) and the evolution of their unit-cell volumes. All the oxides are pure and exhibit the perovskite crystal structure. The volume of the unit cell increases with M in the order $Co^{3+} < Fe^{3+} < Ni^{2+} < Sc^{3+}$, as expected from their ionic radii.[52] Powder Neutron Diffraction (PND) data reveal that all perovskites have monoclinic symmetry with unit-cell parameters $a \neq b \neq c$ and $\alpha = \gamma = 90° \neq \beta$, in the space groups $P2_1/n$ ($a^-a^-c^+$ tilting, Glazer notation) for Ni and Sc oxides, and $I2/m$ ($a^0b^-b^-$ tilting) for Co and Fe oxides.[33,39] Both $P2_1/n$ and $I2/m$ symmetries are characteristic of distorted double perovskites with alternating MO_6 and IrO_6 complexes along the three crystallographic directions in a long-range Oh M/Ir ordering.[53,54]

Oxygen vacancies can play a key role in the OER activity of oxides. Therefore, the presence or absence of oxygen vacancies in the double perovskites was assessed by means of PND. This technique is one of the most reliable ones to evaluate the occupancy of light atoms such as oxygen in oxides.[55] The refinement of the crystal structures reveals the absence of oxygen vacancies in Sr_2MIrO_6, irrespectively of the atom in the M site. PND data also reveal a stoichiometric composition of the catalysts in the bulk.[33,39] The most relevant crystallographic features obtained from PND are detailed in Table S2,† for instance, oxygen vacancies, Ir oxidation state and $\langle Ir–O \rangle$ distances. The surface composition of Sr_2MIrO_6 was studied by XPS, providing a M/Ir ratio close to the nominal value of 1 in all samples. Except for Sr_2NiIrO_6, the surface is enriched in Sr in all of the studied oxides, showing Sr/Ir surface atomic ratios in the range of 1.9 to 3.1. This observation is in line with previous reports on Sr-containing perovskites, where it was reported that $SrCO_3$ forms at the surface.[56]

The oxidation state of M and Ir was studied by XAS and bond-valence sum (BVS) calculations using Brown's model with PND data.[33,39,57] XAS data indicate that Sr_2NiIrO_6 perovskites contain Ni^{2+} and Ir^{6+} cations, whereas the oxidation states in Sr_2CoIrO_6, Sr_2ScIrO_6 and Sr_2FeIrO_6 are close to M^{3+} and Ir^{5+}. However, it should be noted that Ir^{n+} sites are slightly more oxidized in Sr_2CoIrO_6 than in Sr_2FeIrO_6. BVS gives another estimation of the oxidation states using the bond distances calculated from PND, and the results are reliable because the following two conditions were satisfied: (i) lack of disorder between M and Ir cations in both Oh sites, and (ii) absence of oxygen vacancies. The oxidation states obtained using BVS are in good agreement with XAS results, *i.e.*, Fe^{3+}, Sc^{3+} along with the corresponding Ir^{5+} oxidation state; mixed valence Co^{3+}/Co^{2+} (~+2.3) with Ir^{5+}/Ir^{6+} (~+5.7); and finally, Ni^{2+} with Ir^{6+}.

The oxidation state of Ir (and M) at the surface of the perovskites was obtained from XPS. As shown in Fig. S2 in the ESI,† the Ir 4f region can be fitted into two doublets, with $4f_{7/2}$ binding energies at *ca.* 62.5 and 64.5 eV, in good agreement with the XPS analyses of similar Ir perovskites.[18,20,58] It is known that the binding energy of Ir $4f_{7/2}$ in the metallic state appears around 60.33 eV,[59] and increases to values close to 61.8 eV for oxidized Ir (IrO_2).[60] All of the Sr_2MIrO_6 oxides have the main Ir

$4f_{7/2}$ component at binding energies ranging from 62.3 to 62.9 eV, the actual value depending on M. These high binding energies indicate that the double perovskites contain Ir species in oxidation states higher than Ir^{4+}. Similar binding energies were reported for Ba_2PrIrO_6 and La_2LiIrO_6, and ascribed to the presence of Ir^{5+}.[22,23] In agreement with previous works, we believe that it is not possible to obtain the precise oxidation state of the cations at the surface of perovskites based only on XPS data,[22] but the results provided here suffice to conclude that the Ir species at the surface of Sr_2MIrO_6 perovskites have oxidation states higher than +4. In turn, the oxidation states of Ir determine the strength of Ir–O lattice bonds in each compound, and consequently the strength of Ir–adsorbed oxygen bonds, which is a key parameter for describing the OER performance.

3.2 Initial OER activity: effect of M in the catalytic performance

Fig. 1a shows the catalytic activity for the OER of Sr_2MIrO_6 (M = Ni, Co, Sc and Fe) in terms of *iR*-corrected current densities, normalized to the geometric area of the electrodes (0.196 cm^2). The non *iR*-corrected curves and the R obtained from EIS at open-circuit voltage are shown in Fig. S3 and S4 in the ESI.†

The current density decreases with M as $Ni^{2+} > Co^{3+} > Sc^{3+} > Fe^{3+}$. As shown in Table 1, the current densities reached at 1.5 V are 3.3, 2.6, 1.3, and 0.3 mA cm_{disk}^{-2} for Sr_2NiIrO_6, Sr_2CoIrO_6, Sr_2ScIrO_6 and Sr_2FeIrO_6, respectively. The trends can also be observed in the Tafel plots in Fig. 1b.
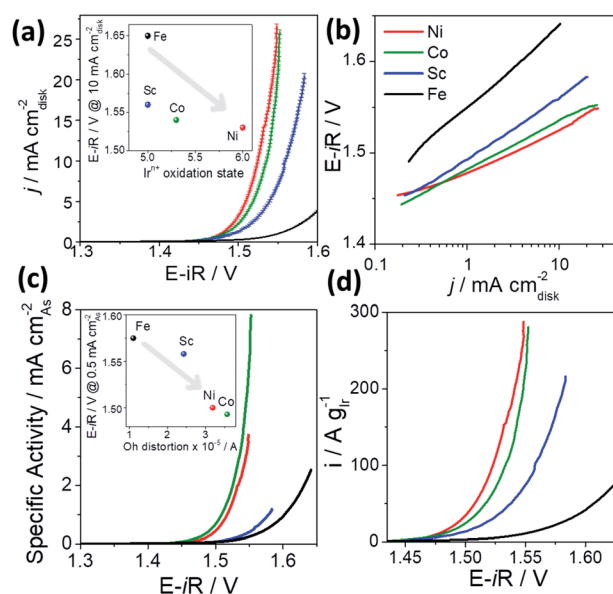

Fig. 1 (a) Current densities of Sr_2MIrO_6 (M = Ni, Co, Sc, Fe). The measurements were performed three or four times and the standard deviations are included in the figure. Inset: OER potential trends at 10 mA cm^{-2} as a function of Ir oxidation state on each catalyst. (b) Tafel plots of Sr_2MIrO_6. (c) Specific activities normalized by mass-specific surface area. Inset: trends in specific activity as a function of the distortion of the IrO_6 Oh across the analyzed perovskites. (d) Mass activity (normalized by grams of Ir) of the perovskites under study.

This journal is © The Royal Society of Chemistry 2021

J. Mater. Chem. A, 2021, **9**, 2980–2990 | **2983**

Table 1 State-of-the-art Ir mixed oxide catalysts for the OER in acid electrolyte

Catalyst	$E - iR$/V@10 mA cm^{-2}	j/mA cm^{-2}@1.5 V	Tafel slope/mV dec^{-1}	Ir/%$_{wt}$	i_M Ag$_{Ir}^{-1}$@1.525 V	Durability tests
Sr_2NiIrO_6	1.525	3.3	48	37	115	1 h@10 mA cm^{-2}
Sr_2CoIrO_6	1.535	2.6	52	37	73	10 000 cycles bt. 1.2–1.7 V@50 mV s^{-1}
Sr_2ScIrO_6	1.56	1.3	67	38	35	1 h@10 mA cm^{-2}
Sr_2FeIrO_6	1.65	0.3	90	37	5.6	1 h@10 mA cm^{-2}
$SrTi_{0.67}Ir_{0.33}O_3$ (ref. 25)	1.477	24	45–80	27	820	20 h@10 mA cm^{-2}
$6H\text{-}SrIrO_3$ (ref. 24)	1.478	12	60–120	58.6	74.7	30 h@10 mA cm^{-2}
$Pr_2Ir_2O_7$ (ref. 28)	1.52	4.5	50	49	351	1000 cycles bt. 1–1.55 V@50 mV s^{-1}
$SrCo_{0.9}Ir_{0.1}O_{3-\delta}$ (ref. 20)	1.55	3.0	40–70	10		3 h@10 mA cm^{-2}
La_2LiIrO_6 (ref. 23)	1.53	0.7	50	33.5	33.5	50 cycles bt. 1.1–1.7 V@10 mV s^{-1}
Ba_2NdIrO_6 (ref. 21)	1.60	0.7	60–130	27		1 h@10 mA cm^{-2}
$Ni_{0.34}Co_{0.46}Ir_{0.2}O_4$ (ref. 30)	1.51	~9	40	34		5.5 h@10 mA cm^{-2}
Sr_2IrO_4 (ref. 31)	1.516	~5	45	44.5	392@1.55 V	6 h@10 mA cm^{-2}
Sr_4IrO_6 (ref. 31)	1.517	~5	50	30.1	274@1.55 V	6 h@10 mA cm^{-2}
IrO_2 (ref. 23)	1.56	0.01	50	86	24.5	

Taking the potential to achieve 10 mA cm^{-2} as an RDE-based metric to benchmark catalysts, as suggested by Jaramillo *et al.*,[61] we observe that Sr_2NiIrO_6 records the least positive potential of 1.525 V, followed by Sr_2CoIrO_6 and Sr_2ScIrO_6, with potentials of 1.535 and 1.560 V, respectively. Clearly, Sr_2NiIrO_6 and Sr_2CoIrO_6 have similar current densities; however, Sr_2ScIrO_6 and Sr_2FeIrO_6 are less active, suggesting that M plays an important role in the OER performance of Sr_2MIrO_6. Sr_2FeIrO_6 records the lowest performance in the whole polarization range, showing a potential of 1.650 V to achieve 10 mA cm^{-2}. Similar OER activity trends have been reported for Sr_2CoIrO_6 and Sr_2FeIrO_6, showing that Co-based catalysts are more active than Fe-based catalysts and that the initial activity is related to the mixed oxide structure.[26]

In Table 1 we compare the electrochemical performance of the perovskites under study with state-of-the-art Ir mixed oxides. Sr_2NiIrO_6, Sr_2CoIrO_6 and Sr_2ScIrO_6 display comparable or higher activity than the best Ir mixed oxides in the literature for the OER in acid media, including $SrCo_{0.9}Ir_{0.1}O_{3-\delta}$,[20] $Pr_2Ir_2O_7$,[27] Ba_2LIrO_6 (L = Y, La, Ce, Pr, Nd, Tb),[21] and La_2LiIrO_6.[23] Sr_2NiIrO_6 and Sr_2CoIrO_6 are only slightly less active than $SrTi_{0.67}Ir_{0.33}O_3$ and 6H-$SrIrO_3$, which have a potential of ~1.47 V at 10 mA cm^{-2}.[24,25] In all cases, it is assumed that Ir sites are the main active sites for the OER, since the overpotentials achieved by Ir mixed oxides are comparable to Ir–O phases.[8,62]

The Tafel slopes obtained at low current densities are also shown in Table 1. The Tafel slopes for Sr_2NiIrO_6 (48 mV dec^{-1}) and Sr_2CoIrO_6 (52 mV dec^{-1}) are in line with the values reported for the best Ir mixed oxides. Indeed, most Ir- and Ru-based catalysts, including IrO_2 and RuO_2, display Tafel slopes between 40 and 60 mV dec^{-1}.[63]

The initial OER activities were first correlated with the oxidation state of the Ir cations in each catalyst (Fig. 1a, inset). The trends in Fig. 1a reveal that the OER activity increases alongside the oxidation state of Ir in the double perovskites. Specifically, Sr_2NiIrO_6 with Ir^{6+} cations displays the highest OER

activity, followed by Sr_2CoIrO_6 with Ir$^{6+/5+}$. The perovskites with Ir^{5+} cations (Sr_2ScIrO_6 and Sr_2FeIrO_6) are the least active ones in the series. The importance of Ir's oxidation state for the OER performance was observed previously in the La_2LiIrO_6 double perovskite.[23] It was claimed that Ir$^{5+}O_6$ Oh are not active for the OER, so that a previous activation step oxidizing Ir^{5+} to Ir^{6+} is needed to make Ir^{5+}-mixed oxides active. This suggests that the higher OER activity of Sr_2NiIrO_6 and Sr_2CoIrO_6 phases could be related to the presence of Ir^{6+} cations. We note that Ir^{6+}–O bonds are shorter and, therefore, more covalent than Ir^{5+}–O bonds. In addition, it has been observed for metals, monoxides and several families of perovskites that, as the oxidation state of the metal centers increases, the adsorption energies of *O, *OH and *OOH become more positive, that is, weaker.[37,64] Hence, we conclude that more covalent Ir–O lattice bonds are concomitant with weaker Ir–*O bonds. It is worth noting here that in a Sabatier-type analysis, the weakening of metal–adsorbate bonds is generally beneficial for the OER when the compounds are initially located on the strong-binding (left) side of a volcano activity plot and until a limit, namely, the top of the volcano. Beyond such limit, the bonds start being undesirably weak, as discussed in the next section.

The specific OER activity of the perovskites was assessed by normalizing the OER activity by the compounds' active surface area (Fig. 1c). The surface area can be calculated by several methods such as BET or electrochemical methods (ECSA). In the case of mixed oxides, in view of their usually low surface areas, it is a common practice to normalize the activity by the mass specific surface area (A_S) calculated from the diameter data of TEM particles (Section S9, ESI†).[14,65] The determination of A_S (eqn (S5) in the ESI†) along with a comparison between A_S, BET and ECSA values is provided in Section S9 in the ESI (Table S3†). The A_S values obtained for the perovskites with M = Ni, Co, Sc and Fe are 2.9, 1.3, 6.8 and 1.6 m^2 g^{-1}, respectively. The different A_S values obtained are in line with the different particle sizes measured, which are 276 ± 29 nm for Ni catalyst,

2984 | *J. Mater. Chem. A*, 2021, **9**, 2980–2990

This journal is © The Royal Society of Chemistry 2021

519 ± 152 nm for Co, 111 ± 33 nm for Sc and 376 ± 110 nm for Fe catalyst.

As observed in Fig. 1c, the specific activities follow a similar trend compared to the current densities, being Sr_2NiIrO_6 and Sr_2CoIrO_6 again the most active OER catalysts. Sr_2CoIrO_6 achieves a specific activity of 7.5 mA cm_{As}^{-2} at 1.55 V, which is larger than the one reported by Grimaud et al.[26] of 4–5 mA cm^{-2} at the same potential. Another important observation is that the specific activities of Sr_2CoIrO_6 and Sr_2FeIrO_6 increase compared to the other catalysts because their surface area is lower. This means that the low current density reached by Sr_2FeIrO_6 stems in part from its low surface area.

We studied the effect that the IrO_6 Oh distortion could have on the OER performance. The Oh distortion (Δ) in perovskites is calculated with eqn (11):[57]

$$\Delta = \frac{1}{6} \sum \{(b_i - b_{av})/b_{av}\}^2 \qquad (11)$$

where b_i are the individual Ir–O distances (taken from ref. 33 and 39) and b_{av} are the average ⟨Ir–O⟩ distances (Table S2†), see Fig. S5 in the ESI.† The inset of Fig. 1c displays the evolution of the potential with the IrO_6 Oh distortion at a specific activity of 0.5 mA cm_{As}^{-2}. We observe that a higher distortion inside the Oh results in higher OER activities. However, Δ gives information about the distortion inside the Oh and not about the tilting of the Oh. Both types of distortions are detailed in Fig. S5 in the ESI.† Concerning the effect of the Oh tilting in the catalytic activity, Fig. S6 in the ESI† illustrates the evolution of the activity on the perovskites under study with the monoclinic β angle and with the Oh tilting itself. Smaller monoclinic β angles indicate that the perovskites are more distorted, i.e., more deviant from the cubic structure. The results indicate that larger Oh tilting also has a positive effect on the OER activity of the perovskites. In conclusion, we observe that both effects, namely higher Oh tilting and higher distortion inside the Oh, result in higher OER activities. We believe that the higher activity of the distorted structures is related to more reactive surfaces. In fact, the effect of the distortions on the stability is the opposite, as discussed in Section 3.5.

Apart from the tuning of the OER activity, one of the main purposes of designing Ir mixed oxides is to decrease the Ir loading on the electrodes. The Ir content of Sr_2MIrO_6 (M = Ni, Co, Sc, Fe) is ca. 38 wt%, which is similar to the content of other Ir mixed oxides and considerably lower than $SrIrO_3$ (59 wt%) and IrO_2 (see Table 1). Regarding the mass activities (in A g_{Ir}^{-1}) of the catalysts (Fig. 1d), we note that the iridium mass fraction of all Sr_2MIrO_6 is similar among the analyzed double perovskites (see Table 1), so the trend is comparable to that of the current densities in Fig. 1a. As shown in Table 1, the mass activities obtained for Sr_2NiIrO_6, Sr_2CoIrO_6 and Sr_2ScIrO_6 at 1.525 V are comparable to state-of-the-art Ir mixed oxides and largely surpass IrO_2.

3.3 Computational modelling of Sr_2MIrO_6 perovskites

To further rationalize the trends in OER catalytic activities of the Sr_2MIrO_6 double perovskites (M = Ni, Co, Sc, Fe), we

resorted to DFT calculations. First, we assessed the bulk configuration of such perovskites. All calculations were performed on antiferromagnetic systems, in line with the experimental antiferromagnetic ordering on these perovskites.[33,39] Among the different antiferromagnetic spin arrangements, we found that the configuration in which the spins are aligned in the (001) plane was most stable for all the analyzed systems.

Furthermore, we calculated the OER overpotentials following the procedure described in the Computational Details section. Values of 0.40, 0.44, 0.75, and 0.79 V were obtained for M = Co, Ni, Fe, and Sc, respectively. Because of the inherent accuracy of DFT (given by the gray bands in Fig. 2a) and the proximity of some of the overpotentials calculated here, we safely conclude that DFT predicts that Sr_2MIrO_6 with Co and Ni are more active than those with Fe and Sc, in agreement with experiments. However, it is difficult to ascertain if double perovskites with Co are more active than those with Ni. We note as well that depending on the activity metrics, the ordering between M = Co and Ni changes, see Fig. 1a and c. These results are in line with the experimental observations in Fig. 1b. We rationalize the trends in two different ways. Firstly, in Fig. 2a, the overpotentials of the studied perovskites appear as a function of the descriptor $\Delta G_O - \Delta G_{OH}$, which renders a volcano-type activity plot for the OER.[43,44] For the sake of comparison, we also
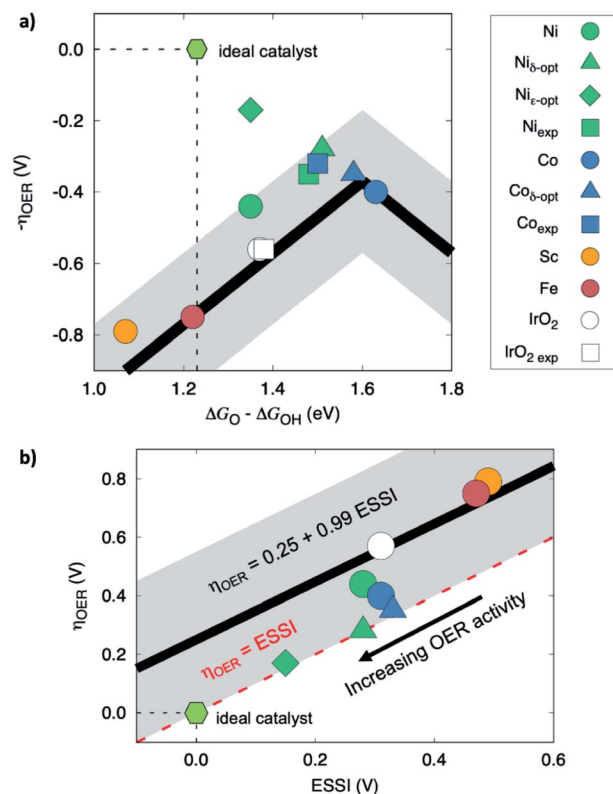

Fig. 2 Computational modelling of the OER on Sr_2MIrO_6 with M = Ni, Co, Sc, Fe. (a) Volcano-type activity plot. Experimental data added following a method described previously.[67,68] (b) OER overpotential as a function of the electrochemical-step symmetry index (ESSI). Optimized data calculated using the $\delta-\varepsilon$ method in ref. 47 The ideal catalyst and $IrO_2(110)$ are provided for comparison.[44,66]

This journal is © The Royal Society of Chemistry 2021

J. Mater. Chem. A, 2021, **9**, 2980–2990 | **2985**

included computational[44] and experimental[66] literature data for IrO_2, together with Sr_2CoIrO_6 and Sr_2NiIrO_6 from our own experimental data (the addition of experimental data into the computational volcano plot is made following the method described elsewhere[67,68]). Fig. 2a shows that the double perovskites follow the traditional adsorption-energy scaling relations, and those with M = Co, Ni are the closest to the top of the volcano, even surpassing $IrO_2(110)$. Since most of the compounds in Fig. 2a are on the left (strong-binding) side of the volcano, weakening the adsorption energy of *O likely enhances the activity.

Secondly, from a thermodynamic standpoint the ultimate goal in OER electrocatalysis is to reach thermoneutrality,[46,69,70] which is achieved by a hypothetical "ideal" catalyst for a multi-electron reaction. The OER reaction steps of such catalyst are fully symmetric, that is, with $\Delta G_i = 1.23$ eV (eqn (5)–(8)), which implies that $\eta_{OER} = 0$ V. To quantify how much a real catalyst approaches the ideal catalyst, one can use the electrochemical-step symmetry index (ESSI, see the Computational Details section).[46] This metric for electrocatalytic symmetry is defined so that the OER overpotential is reduced as the symmetry of catalysts increases, namely when ESSI approaches zero. The studied Sr_2MIrO_6 compounds comply with this general guideline in Fig. 2b, where we observe a good correspondence between ESSI and η_{OER}. The OER at Ir sites seems rather asymmetric when Sc and Fe are in the M position of Sr_2MIrO_6, whereas Co and Ni help increase the electrocatalytic symmetry, thereby lowering the OER overpotential.

An interesting feature of ESSI is its ability to provide guidelines for the enhancement of electrocatalysts.[47] This can be made following adsorption-energy scaling relations between *O, *OH and *OOH, or breaking them, respectively referred to as δ and ε optimization. The triangles in Fig. 2a and b show that

the scaling-based δ-optimization of double perovskites with Ni would sizably reduce η_{OER} from 0.44 to 0.28 V if *OH binding energies decrease by 0.16 eV. Double perovskites with Co would only experience a small reduction from 0.40 to 0.35 V when *OH adsorption be strengthened by 0.05 eV. On the other hand, scaling-free ε-optimization would only benefit Sr_2NiIrO_6, for which a strengthening of 0.27 eV in *OOH adsorption with respect to *OH would lower the overpotential to 0.17 V. All this implies that Sr_2NiIrO_6 is more prone to further optimization, which is interesting for future studies.

3.4 Studying the initial OER activity of Ir double perovskites

Both the experimental and theoretical results presented in this work indicate that Sr_2CoIrO_6 and Sr_2NiIrO_6 are the most active catalysts among the studied Ir double perovskites. To verify that the initial OER activities reported in Fig. 1 can be ascribed to the perovskite phase and not to IrO_x/IrOOH surface segregated phases, we characterized the most active perovskites (Sr_2CoIrO_6 and Sr_2NiIrO_6) after 5 cycles in OER by TEM/EDX and XPS. We specifically chose 5 cycles because no significant changes on the current densities are observed after those. The HRTEM images shown in Fig. 3a, which correspond to the catalysts recovered after 5 cycles, indicate that the materials still display the perovskite structure with only a minor fraction of Ir particles observed at the surface.

We studied the surface of Sr_2CoIrO_6 and Sr_2FeIrO_6 perovskites by XPS before and after 5 cycles of reaction to compare the surface stability of a highly active catalyst and one with considerably lower activity. Both samples present Sr, Ir and M cations with Ir/M surface atomic ratios close to the initial nominal value of 1. However, the content of Sr is significantly smaller after 5 cycles than that on the initial samples (Fig. 3b),
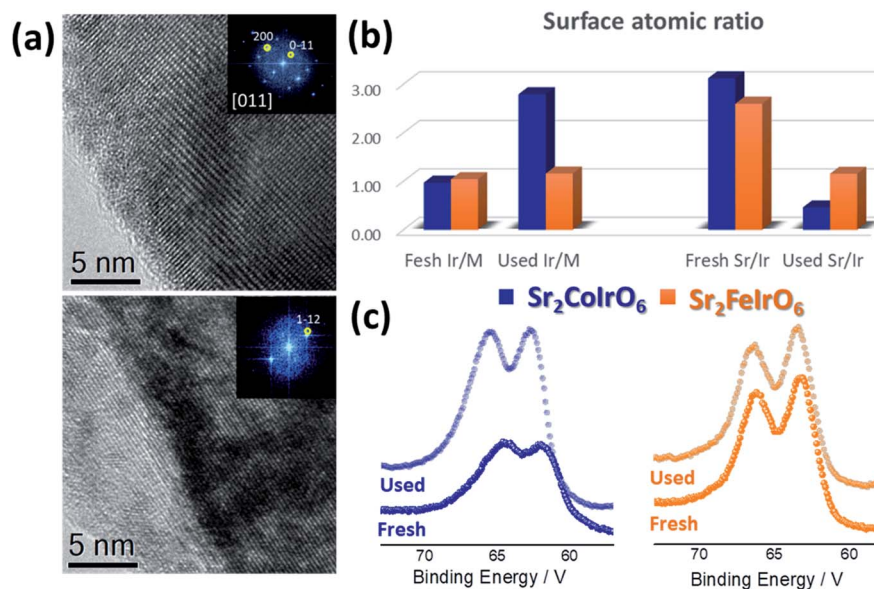

Fig. 3 (a) HRTEM images after 5 OER cycles for Sr_2NiIrO_6 perovskite (upper) oriented along the [011] zone axis and Sr_2CoIrO_6 (lower) where the [1-12] planes of the perovskite can be seen. (b) Sr, M and Ir surface content on Sr_2CoIrO_6 and Sr_2FeIrO_6 before and after 5 OER cycles determined by XPS. (c) XPS Ir 4f region of Sr_2CoIrO_6 and Sr_2FeIrO_6 before and after 5 OER cycles in acid media.

2986 | J. Mater. Chem. A, 2021, **9**, 2980–2990

This journal is © The Royal Society of Chemistry 2021

reflecting the high tendency of Sr to dissolve in the electrolyte. In the case of Sr_2CoIrO_6, the surface content of Ir increased compared to the content of M (Fig. 3b), indicating the incipient formation of Ir-based nanoparticles.

We also analyzed the evolution of the XPS-Ir 4f region (Fig. 3c). According to previous reports dealing with the stability of Ir perovskites for the OER in acid electrolyte,[23] if the used perovskites were covered by IrO_x/IrOOH nanoparticles, the oxidation state of Ir would change to +4/+3 after the reaction. However, as observed in Fig. 3c, the Ir 4f core-level region is not shifted to smaller binding energies (as expected for a reduction in Ir's oxidation state) after 5 OER cycles. Instead, it remains at the same binding energy for Sr_2FeIrO_6, or shifts to slightly higher binding energies for Sr_2CoIrO_6. In line with a previous report,[23] we suggest that the oxidation from Ir^{5+} to Ir^{6+} is responsible for the high OER activity Sr_2CoIrO_6. This partial surface oxidation of Ir during the OER has been observed and correlated with an activity enhancement, owed to the existence of Ir in a higher oxidation state or a different molecular surface environment, caused by the oxidizing conditions of the OER.[18,31] On the other hand, the oxidation of Ir^{5+} to Ir^{6+} is not observed in Sr_2FeIrO_6, which exhibits lower OER activity but higher stability (see below). These observations clearly indicate that the oxidation state of Ir plays a crucial role in the OER activity, which seems to be enhanced by Ir cations with upper oxidation states.

3.5 Stability and evolution of Sr_2MIrO_6 during the OER

The instability of mixed oxides during the OER in acidic media is an issue yet to be resolved. It has been reported that mixed oxides lose stability after several OER cycles, sometimes immediately after immersion in the electrolyte, prior to the OER

cycling experiments.[20,22,23,38] This lack of stability leads to catalysts that are more active than the fresh mixed oxide, likely due to the deposition of highly active IrO_x/IrOOH nanosized particles at the surface of the mixed oxides. As shown in Fig. 3, we tested the catalysts after 5 cycles of reaction and, although the perovskite was still the main phase, some signs of degradation were observed. To further evaluate the stability of Sr_2MIrO_6, we measured 50 OER cycles at 10 mV s^{-1} between 1.2 and 1.7 V (Fig. 4a), in all cases showing an increment of the OER activity with cycling. To understand the origin of the observed behavior, we analyzed the structure and composition of the used catalysts after such 50 cycles.

Fig. 4b shows representative HRTEM images of the perovskites after 50 OER cycles. The structure of Sr_2CoIrO_6 and Sr_2NiIrO_6 collapses, as observed in the HRTEM and in the FFT in the inset. The resulting material is formed by nanometric Ir-based particles with no signal indicative of the presence of Co, Ni or Sr in the samples after 50 cycles (EDX results, Fig. S8 in the ESI†). However, the morphology of both catalysts after 50 cycles is different (Fig. S9 in the ESI†). The Ni-containing catalyst collapses into a more open structure, less dense and apparently with more surface area (Fig. S9a†), while the Co-containing catalyst presents a more compact morphology (Fig. S9b†).

On the other hand, Sr_2FeIrO_6 and Sr_2ScIrO_6 maintain the perovskite structure as suggested by the presence of the (101) perovskite planes in the Sc perovskite and the oriented structure down the [111] zone axis in the case of the Fe-containing double perovskite. The presence of Sr, Fe(Sc) and Ir in the particles can be observed by EDX analyses, see the map in Fig. 4c. However, a careful analysis of the used perovskites also reveals the presence of IrO_x nanoparticles at the surface of the latter perovskites (Fig. 4b), indicating the reconstruction of the perovskites during the OER. These results suggest that, contrary to the activity trend, the more distorted perovskites (M = Co and Ni) are less stable than the more symmetric ones (M = Sc and Fe).

Insights onto the deactivation of representative Sr_2CoIrO_6 and Sr_2FeIrO_6 samples were obtained by analysing the composition of the electrolyte by ICP-OES. We collected electrolyte before the reaction and after 5 and 50 OER cycles. The evolution of Sr, M (Co and Fe) and Ir concentrations in the electrolyte during the OER with both catalysts is shown in Fig. S10 in the ESI.† As observed, Sr and M dissolve faster in Sr_2CoIrO_6 than in Sr_2FeIrO_6 with cycling, indicating that Sr_2FeIrO_6 is more stable for the OER in acid electrolyte. In both cases the dissolution of Ir is low, in agreement with the formation of IrO_x particles at the surface that are not dissolved during the reaction.

These observations are in good agreement with previous studies,[36,71] reporting that more symmetric perovskites are more stable under the conditions of the H_2O/O_2 interconversion reactions, since they can be subjected to more extreme potentials without being destroyed. Conversely, distorted structures are susceptible to dissolution upon OER cycling.

We also performed chronoamperometry studies during one hour at the fixed potential where the current density is 10 mA cm^{-2} (Fig. 5a). The double perovskites' activity is stable during such steady-state durability test, losing only 5–10% of the initial
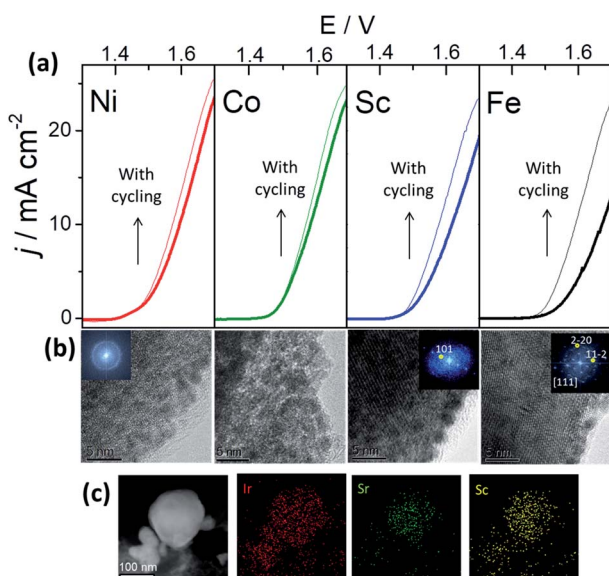

Fig. 4 (a) OER CV voltammetries. The figure shows the first (thick lines) and 50th (thin lines) cycles for all the perovskites under study. (b) HRTEM images of Sr_2MIrO_6 samples (Ni, Co, Sc and Fe from left to right) after 50 OER cycles. (c) EDX mapping for Sr_2ScIrO_6 after 50 cycles.

activity in all cases. This result indicates the easier formation of Ir-nanoparticles on the surface during cycling experiments compared to experiments performed at a selected current density (*i.e.* 10 mA cm^{-2}).

In view of the high OER activity of Sr_2NiIrO_6 and Sr_2CoIrO_6, we performed a more aggressive dynamic durability test consisting of 10 000 OER cycles at 50 mV s^{-1} between 1.2 and 1.7 V (Fig. 5b) on both catalysts. This stability test is essentially an experiment in which the catalysts are continuously cycled between those two potentials in acid media for ∼55 h. In the case of Sr_2NiIrO_6, the activity loss after 10 000 cycles is small, with an increment of potential of only 10 mV to achieve the reference current density of 10 mA cm^{-2}. For Sr_2CoIrO_6, the activity decreases from 13.3 to 9.8 mA cm^{-2} at 1.6 V, indicating severe deactivation after the durability test. The activity loss on Sr_2CoIrO_6 can also be followed from the evolution of the potential needed to achieve a current density of 10 mA cm^{-2}, which increases from 1.57 to 1.60 V. These results may indicate that the surface reconstruction is different in both oxides. The effect of different surface reconstruction on the OER durability has been extensively reported.[20,22–24,72] Analyzing the reconstruction of the surface after 50 cycles for both oxides (Fig. S9 in the ESI†), we conclude that the Ni-containing catalyst presents less dense Ir phases than the Co-containing catalyst. This different morphology can explain the different evolution of the catalyst after the long-term durability test. Probably, during

cycling, the Co-containing catalyst forms larger Ir particles more rapidly than the Ni-containing catalyst, decreasing its current density after 10 000 cycles.

4. Conclusions

In this study we report the performance of Sr_2MIrO_6 (M = Ni, Co, Sc, Fe) double perovskites for the OER in acid electrolyte and rationalize the trends using a variety of experimental and computational descriptors, such as Ir oxidation state, degree of octahedral distortion, strength of Ir–adsorbate bonds, and electrocatalytic symmetry. The OER activities are comparable to those of state-of-the-art Ir-based catalysts, following the trend $Sr_2FeIrO_6 < Sr_2ScIrO_6 < Sr_2CoIrO_6 < Sr_2NiIrO_6$. The higher OER activity of Sr_2NiIrO_6 and Sr_2CoIrO_6 stems from their ability to stabilize Ir^{6+} cations during the OER. However, the stability of both oxides is lower than those of Sr_2ScIrO_6 and Sr_2FeIrO_6 in which lower Ir oxidation states are found. Thus, low Ir oxidation states, relatively strong binding energies and high structural symmetry ensure high stability.

While all of the analyzed materials exhibit the perovskite structure during the first cycles of reaction, only the more symmetric phases, which are the lesser active, maintain the perovskite structure for more than 50 OER reaction cycles.

The correlations between iridium oxidation state, adsorption energies and OER activity in acid media reported in this work can serve as a guideline for designing more active and durable OER catalysts in acid electrolyte. Our results hint toward a necessary tradeoff between activity and stability, which can be provided by a careful selection of the metal M in Sr_2MIrO_6 double perovskites.

Conflicts of interest

There are no conflicts to declare.

Acknowledgements

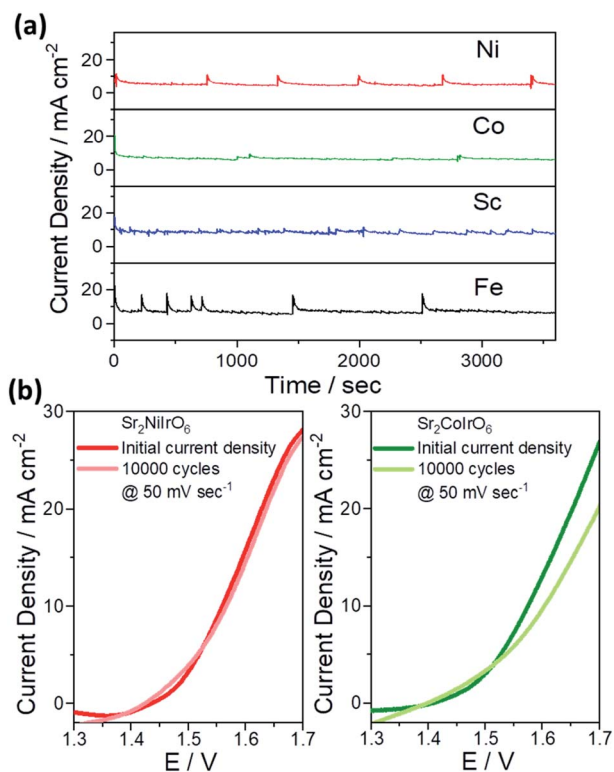**Fig. 5** (a) Chronoamperometries at the potentials where j = 10 mA cm^{-2}, which are *ca.* 1.52, 1.53, 1.56 and 1.64 V (*iR* corrected) for M = Ni, Co, Sc, Fe, respectively. (b) 10 000 OER cycles at 50 mV s^{-1} for Sr_2-NiIrO$_6$ and Sr_2CoIrO_6, compared to their initial current density.

2988 | *J. Mater. Chem. A*, 2021, **9**, 2980–2990

This journal is © The Royal Society of Chemistry 2021

References

1 V. R. Stamenkovic, D. Strmcnik, P. P. Lopes and N. M. Markovic, *Nat. Mater.*, 2017, **16**, 57–69.

2 B. C. H. Steele and A. Heinzel, *Nature*, 2001, **414**, 345–352.

3 O. Schmidt, A. Gambhir, I. Staffell, A. Hawkes, J. Nelson and S. Few, *Int. J. Hydrogen Energy*, 2017, **42**, 30470–30492.

4 M. Carmo, D. L. Fritz, J. Mergel and D. Stolten, *Int. J. Hydrogen Energy*, 2013, **38**, 4901–4934.

5 I. Katsounaros, S. Cherevko, A. R. Zeradjanin and K. J. J. Mayrhofer, *Angew. Chem., Int. Ed.*, 2014, **53**, 102–121.

6 K. Zeng and D. Zhang, *Prog. Energy Combust. Sci.*, 2010, **36**, 307–326.

7 N. Hodnik, P. Jovanovič, A. Pavlišič, B. Jozinović, M. Zorko, M. Bele, V. S. Šelih, M. Šala, S. Hočevar and M. Gaberšček, *J. Phys. Chem. C*, 2015, **119**, 10140–10147.

8 D. F. Abbott, D. Lebedev, K. Waltar, M. Povia, M. Nachtegaal, E. Fabbri, C. Copéret and T. J. Schmidt, *Chem. Mater.*, 2016, **28**, 6591–6604.

9 C. Rozain, E. Mayousse, N. Guillet and P. Millet, *Appl. Catal., B*, 2016, **182**, 153–160.

10 H. N. Nong, H. S. Oh, T. Reier, E. Willinger, M. G. Willinger, V. Petkov, D. Teschner and P. Strasser, *Angew. Chem., Int. Ed.*, 2015, **54**, 2975–2979.

11 P. Lettenmeier, L. Wang, U. Golla-Schindler, P. Gazdzicki, N. A. Cañas, M. Handl, R. Hiesgen, S. S. Hosseiny, A. S. Gago and K. A. Friedrich, *Angew. Chem., Int. Ed.*, 2016, **55**, 742–746.

12 H. Yu, N. Danilovic, Y. Wang, W. Willis, A. Poozhikunnath, L. Bonville, C. Capuano, K. Ayers and R. Maric, *Appl. Catal., B*, 2018, **239**, 133–146.

13 E. Antolini, *ACS Catal.*, 2014, **4**, 1426–1440.

14 J. Suntivich, K. J. May, H. A. Gasteiger, J. B. Goodenough and Y. Shao-Horn, *Science*, 2011, **334**, 1383–1385.

15 A. Grimaud, K. J. May, C. E. Carlton, Y.-L. Lee, M. Risch, W. T. Hong, J. Zhou and Y. Shao-Horn, *Nat. Commun.*, 2013, **4**, 2439.

16 C. Sun, J. A. Alonso and J. Bian, *Adv. Energy Mater.*, 2020, 2000459, 1–21.

17 J. Bian, Z. Li, N. Li and C. Sun, *Inorg. Chem.*, 2019, **58**, 8208–8214.

18 L. C. Seitz, C. F. Dickens, K. Nishio, Y. Hikita, J. Montoya, A. Doyle, C. Kirk, A. Vojvodic, H. Y. Hwang, J. K. Norskov and T. F. Jaramillo, *Science*, 2016, **353**, 1011–1014.

19 R. Tang, Y. Nie, J. K. Kawasaki, D. Y. Kuo, G. Petretto, G. Hautier, G. M. Rignanese, K. M. Shen, D. G. Schlom and J. Suntivich, *J. Mater. Chem. A*, 2016, **4**, 6831–6836.

20 Y. Chen, H. Li, J. Wang, Y. Du, S. Xi, Y. Sun, M. Sherburne, J. W. Ager, A. C. Fisher and Z. J. Xu, *Nat. Commun.*, 2019, **10**, 572.

21 O. Diaz-Morales, S. Raaijman, R. Kortlever, P. J. Kooyman, T. Wezendonk, J. Gascon, W. T. Fu and M. T. M. Koper, *Nat. Commun.*, 2016, **7**, 12363.

22 S. Geiger, O. Kasian, M. Ledendecker, E. Pizzutilo, A. M. Mingers, W. T. Fu, O. Diaz-Morales, Z. Li, T. Oellers, L. Fruchter, A. Ludwig, K. J. J. Mayrhofer, M. T. M. Koper and S. Cherevko, *Nat. Catal.*, 2018, **1**, 508–515.

23 A. Grimaud, A. Demortière, M. Saubanère, W. Dachraoui, M. Duchamp, M.-L. Doublet and J.-M. Tarascon, *Nat. Energy*, 2017, **2**, 16189.

24 L. Yang, G. Yu, X. Ai, W. Yan, H. Duan, W. Chen, X. Li, T. Wang, C. Zhang, X. Huang, J.-S. Chen and X. Zou, *Nat. Commun.*, 2018, **9**, 5236.

25 X. Liang, L. Shi, Y. Liu, H. Chen, R. Si, W. Yan, Q. Zhang, G. D. Li, L. Yang and X. Zou, *Angew. Chem., Int. Ed.*, 2019, **58**, 7631–7635.

26 R. Zhang, N. Dubouis, M. Ben Osman, W. Yin, M. T. Sougrati, D. A. D. Corte, D. Giaume and A. Grimaud, *Angew. Chem.*, 2019, **131**, 4619–4623.

27 W. Sun, J. Y. Liu, X. Q. Gong, W. Q. Zaman, L. M. Cao and J. Yang, *Sci. Rep.*, 2016, **6**, 1–10.

28 C. Shang, C. Cao, D. Yu, Y. Yan, Y. Lin, H. Li, T. Zheng, X. Yan, W. Yu, S. Zhou and J. Zeng, *Adv. Mater.*, 2019, **31**, 1–6.

29 D. Lebedev, M. Povia, K. Waltar, P. M. Abdala, I. E. Castelli, E. Fabbri, M. V. Blanco, A. Fedorov, C. Copéret, N. Marzari and T. J. Schmidt, *Chem. Mater.*, 2017, **29**, 5182–5191.

30 W. Q. Zaman, W. Sun, M. Tariq, Z. Zhou, U. Farooq, Z. Abbas, L. Cao and J. Yang, *Appl. Catal., B*, 2019, **244**, 295–302.

31 A. L. Strickler, D. Higgins and T. F. Jaramillo, *ACS Appl. Energy Mater.*, 2019, **2**, 5490–5498.

32 D. Y. Jung, G. Demazeau and J. H. Choy, *J. Mater. Chem.*, 1995, **5**, 517–519.

33 P. Kayser, J. A. Alonso, F. J. Mompeán, M. Retuerto, M. Croft, A. Ignatov and M. T. Fernández-Díaz, *Eur. J. Inorg. Chem.*, 2015, **2015**, 5027–5038.

34 P. Kayser, M. J. Martínez-Lope, J. A. Alonso, M. Retuerto, M. Croft, A. Ignatov and M. T. Fernández-Díaz, *Eur. J. Inorg. Chem.*, 2014, **2014**, 178–185.

35 Y. L. Lee, J. Kleis, J. Rossmeisl, S. H. Yang and D. Morgan, *Energy Environ. Sci.*, 2011, **4**, 3966–3970.

36 W. T. Hong, M. Risch, K. A. Stoerzinger, A. Grimaud, J. Suntivich and Y. Shao-Horn, *Energy Environ. Sci.*, 2015, **8**, 1404–1427.

37 F. Calle-Vallejo, N. G. Inoglu, H. Y. Su, J. I. Martínez, I. C. Man, M. T. M. Koper, J. R. Kitchin and J. Rossmeisl, *Chem. Sci.*, 2013, **4**, 1245–1249.

38 T. Reier, Z. Pawolek, S. Cherevko, M. Bruns, T. Jones, D. Teschner, S. Selve, A. Bergmann, H. N. Nong, R. Schlögl, K. J. J. Mayrhofer and P. Strasser, *J. Am. Chem. Soc.*, 2015, **137**, 13031–13040.

39 P. Kayser, M. J. Martínez-Lope, J. A. Alonso, M. Retuerto, M. Croft, A. Ignatov and M. T. Fernández-Díaz, *Inorg. Chem.*, 2013, **52**, 11013–11022.

40 G. Kresse and J. Furthmüller, *Phys. Rev. B: Condens. Matter Mater. Phys.*, 1996, **54**, 11169–11186.

41 B. Hammer, L. B. Hansen and J. K. Nørskov, *Phys. Rev. B: Condens. Matter Mater. Phys.*, 1999, **59**, 7413–7421.

42 D. Joubert, *Phys. Rev. B: Condens. Matter Mater. Phys.*, 1999, **59**, 1758–1775.

This journal is © The Royal Society of Chemistry 2021

J. Mater. Chem. A, 2021, **9**, 2980–2990 | **2989**

43 J. Rossmeisl, Z. W. Qu, H. Zhu, G. J. Kroes and J. K. Nørskov, *J. Electroanal. Chem.*, 2007, **607**, 83–89.

44 I. C. Man, H. Y. Su, F. Calle-Vallejo, H. A. Hansen, J. I. Martínez, N. G. Inoglu, J. Kitchin, T. F. Jaramillo, J. K. Nørskov and J. Rossmeisl, *ChemCatChem*, 2011, **3**, 1159–1165.

45 J. K. Nørskov, J. Rossmeisl, A. Logadottir, L. Lindqvist, J. R. Kitchin, T. Bligaard and H. Jónsson, *J. Phys. Chem. B*, 2004, **108**, 17886–17892.

46 N. Govindarajan, J. M. García-Lastra, E. J. Meijer and F. Calle-Vallejo, *Curr. Opin. Electrochem.*, 2018, **8**, 110–117.

47 N. Govindarajan, M. T. M. Koper, E. J. Meijer and F. Calle-Vallejo, *ACS Catal.*, 2019, **9**, 4218–4225.

48 Z. Xu and J. R. Kitchin, *Phys. Chem. Chem. Phys.*, 2015, **17**, 28943–28949.

49 Z. Xu, J. Rossmeisl and J. R. Kitchin, *J. Phys. Chem. C*, 2015, **119**, 4827–4833.

50 L. G. V. Briquet, M. Sarwar, J. Mugo, G. Jones and F. Calle-Vallejo, *ChemCatChem*, 2017, **9**, 1261–1268.

51 C. F. Dickens and J. K. Nørskov, *J. Phys. Chem. C*, 2017, **121**, 18516–18524.

52 R. D. Shannon, *Acta Crystallogr., Sect. A: Cryst. Phys., Diffr., Theor. Gen. Crystallogr.*, 1976, **32**, 751–767.

53 M. Retuerto, J. A. Alonso, M. García-Hernández and M. J. Martínez-Lope, *Solid State Commun.*, 2006, **139**, 19–22.

54 T. Stoyanova-Lyubenova, A. J. Dos santos-García, E. Urones-Garrote, M. J. Torralvo and M. Á. Alario-Franco, *Dalton Trans.*, 2014, **43**, 1117–1124.

55 M. Retuerto, A. G. Pereira, F. J. Pérez-Alonso, M. A. Peña, J. L. G. Fierro, J. A. Alonso, M. T. Fernández-Díaz, L. Pascual and S. Rojas, *Appl. Catal., B*, 2017, **203**, 363–371.

56 M. Retuerto, F. Jiménez-Villacorta, M. J. Martínez-Lope, Y. Huttel, E. Roman, M. T. Fernández-Díaz and J. A. Alonso, *Phys. Chem. Chem. Phys.*, 2010, **12**, 13616.

57 I. D. Brown and R. D. Shannon, *Acta Crystallogr.*, 1973, **29**, 266.

58 A. Grimaud, O. Diaz-Morales, B. Han, W. T. Hong, Y. L. Lee, L. Giordano, K. A. Stoerzinger, M. T. M. Koper and Y. Shao-Horn, *Nat. Chem.*, 2017, **9**, 457–465.

59 M. Peuckert, *Surf. Sci.*, 1984, **144**, 451–464.

60 V. Pfeifer, T. E. Jones, J. J. Velasco Vélez, C. Massué, M. T. Greiner, R. Arrigo, D. Teschner, F. Girgsdies, M. Scherzer, J. Allan, M. Hashagen, G. Weinberg, S. Piccinin, M. Hävecker, A. Knop-Gericke and R. Schlögl, *Phys. Chem. Chem. Phys.*, 2016, **18**, 2292–2296.

61 C. C. L. McCrory, S. Jung, J. C. Peters and T. F. Jaramillo, *J. Am. Chem. Soc.*, 2013, **135**, 16977–16987.

62 T. Reier, M. Oezaslan and P. Strasser, *ACS Catal.*, 2012, **2**, 1765–1772.

63 Y. Lee, J. Suntivich, K. J. May, E. E. Perry and Y. Shao-Horn, *J. Phys. Chem. Lett.*, 2012, **3**, 399–404.

64 F. Calle-Vallejo, O. A. Díaz-Morales, M. J. Kolb and M. T. M. Koper, *ACS Catal.*, 2015, **5**, 869–873.

65 J. Suntivich, H. A. Gasteiger, N. Yabuuchi and Y. Shao-Horn, *J. Electrochem. Soc.*, 2010, **157**, B1263.

66 K. A. Stoerzinger, L. Qiao, M. D. Biegalski and Y. Shao-Horn, *J. Phys. Chem. Lett.*, 2014, **5**, 1636–1641.

67 Z. W. Seh, J. Kibsgaard, C. F. Dickens, I. Chorkendorff, J. K. Nørskov and T. F. Jaramillo, *Science*, 2017, **355**, eaad4998.

68 M. Retuerto, L. Pascual, F. Calle-Vallejo, P. Ferrer, D. Gianolio, A. G. Pereira, Á. García, J. Torrero, M. T. Fernández-Díaz, P. Bencok, M. A. Peña, J. L. G. Fierro and S. Rojas, *Nat. Commun.*, 2019, **10**, 2041.

69 C. H. Kjaergaard, J. Rossmeisl and J. K. Nørskov, *Inorg. Chem.*, 2010, **49**, 3567–3572.

70 M. T. M. Koper, *J. Electroanal. Chem.*, 2011, **660**, 254–260.

71 J. Suntivich, H. A. Gasteiger, N. Yabuuchi, H. Nakanishi, J. B. Goodenough and Y. Shao-Horn, *Nat. Chem.*, 2011, **3**, 546–550.

72 C. W. Song, J. Lim, H. Bin Bae and S.-Y. Chung, *Energy Environ. Sci.*, 2020, **13**, 4178–4188.